Interface bonding properties of polyvinyl alcohol (PVA) fiber in alkali-activated slag/fly ash

Zhang, Shizhe; He, Shan; Ghiassi, Bahman; van Breugel, Klaas; Ye, Guang

DOI
10.1016/j.cemconres.2023.107308

Publication date
2023

Document Version
Accepted author manuscript

Published in
Cement and Concrete Research

Citation (APA)
Zhang, S., He, S., Ghiassi, B., van Breugel, K., & Ye, G. (2023). Interface bonding properties of polyvinyl alcohol (PVA) fiber in alkali-activated slag/fly ash. *Cement and Concrete Research*, *173*, Article 107308. https://doi.org/10.1016/j.cemconres.2023.107308

Interface bonding properties of polyvinyl alcohol (PVA) fiber in alkali-activated slag/fly ash

Shizhe Zhang[1, 2, *], Shan He[1], Bahman Ghiassi[3], Klaas van Breugel[1], Guang Ye[1, **]

[1]Microlab, Section Materials and Environment, Faculty of Civil Engineering and Geosciences, Delft University of Technology, Stevinweg 1, 2628 CN, Delft, the Netherlands

[2]Renewi Mineralz & Water, Vlasweg 12, 4782 PW, Moerdijk, the Netherlands

[3]School of Engineering, University of Birmingham, B15 2TT, Birmingham, United Kingdom

Corresponding author email:

[*]Shizhe.Zhang@tudelft.nl

[**]G.Ye@tudelft.nl

Keywords: bonding; interface; fiber pullout; PVA; alkali-activation; slag; fly ash

Abstract

This paper presents an experimental study on the interface bonding properties of polyvinyl alcohol (PVA) fiber in alkali-activated slag/fly ash (AASF) pastes. Three interface bonding properties (i.e., the chemical bonding energy G_d, the initial frictional bond strength τ_0, and slip-hardening behavior β) were determined using single-fiber pullout tests. The microstructure and chemical composition of the reaction products in the fiber/matrix interfacial transition zone (ITZ) and the nearby matrix were also characterized to reveal the influence of PVA fiber to its surrounding matrix. It is found that G_d increases primarily with increasing Ca/(Si+Al) ratio of C-(N-)A-S-H gel. Unlike that in cementitious materials, the inclusion of PVA fiber in AASF pastes promotes the formation of a high-Ca C-(N-)A-S-H phase rather than crystalline portlandite near the fiber surface. This study provides useful guidance for tailoring the interface bonding properties of AASF and also the development of high-performance composites such as strain-hardening geopolymer composites.

1. Introduction

Alkali-activation is one of the few technologies that can transform wastes and industrial by-products into cement-free building materials. Alkali-activated materials (AAMs) including those classified as geopolymer are derived by the reaction of an alkali metal source (solid or dissolved) with a solid alumino-silicate powder [1, 2]. With proper mixture design, they can provide significant environmental benefits, particularly regarding the reduction of CO_2 emissions and energy consumption [3-5].

Furthermore, AAMs as binder material for concrete could maintain comparable mechanical properties and even better durability under certain exposure conditions [6-9]. Among all AAMs, the ones based on blast furnace slag, class F fly ash, and their blends are the most intensively studied [10]. This is mainly due to the large quantity of annual production as well as the relatively stable chemical compositions of these two solid precursors [1, 2, 11, 12]. Previous studies on the slag/fly ash-based AAMs, namely alkali-activated slag/fly ash (AASF), have focused on microstructure development, nature of reaction products as well as mechanical properties [13-18]. The application of AASF for engineering practices has also been greatly promoted.

Like conventional cementitious binders, AAMs are also inherently (quasi-)brittle and thereby susceptible to cracking [19-22]. As one of the classic approaches to control brittleness, fiber reinforcement has been researched in AAMs and was found to hold promise in achieving advanced fracture and tensile performances [23-26]. Polymeric micro-fibers were used to effectively obtain a composite with extraordinary tensile performance, among which, polyvinyl alcohol (PVA) fiber with good bonding to hydration products and sound mechanical properties has been widely used [23-26]. Particularly, it is applied for the development of high-performance composites such as strain-hardening cementitious composite (SHCC) [27] and strain-hardening geopolymer composite (SHGC) [23-25].

For the development of PVA fiber-reinforced cementitious and/or alkali-activated composites, the fiber/matrix interface bonding properties are crucial. Many previous studies thereby focused on the characterization and modification of the PVA fiber/matrix interface by performing single-fiber pullout tests [28-30]. However, the interface bonding properties of PVA fiber within AAMs are not sufficiently investigated. Only a few experimental studies could be found. For instance, Ohno and Li [23] researched the interface properties of PVA fiber in a fly ash-based geopolymer matrix. They found that, in comparison to those in conventional SHCC materials, the chemical bonding G_d is almost 5 times stronger while the frictional bond and tendency for slip-hardening behavior is considerably weaker. Nematollahi et al. [24] tested the interface properties of PVA fiber/matrix properties in alkali-activated fly ash mixtures. The influence of using both sodium and potassium silicate-based activators and the surface oiling treatment on the interface properties were addressed. Compared to the sodium-based activator, the potassium silicate-based ones significantly enhance the chemical bond while weakening the frictional bond and slip-hardening. Similar findings have also been confirmed by Trindade et al. in the study of PVA fiber in metakaolin-based systems [31]. Additionally, Nematollahi et al. [26] concluded that the strong chemical bonding of PVA fiber within a one-part AASF matrix could effectively enhance the fiber-bridging strength of the composite. Zhang et al. [25] tested the interface bonding properties of PVA fiber in AASF matrices and reported that the chemical bonding could be effectively modified by changing the silicate modulus of the alkaline activator. Furthermore, with the help of molecular dynamics (MD) simulation, they also found that adhesion between PVA

fiber surface and the reaction products in AASF is mainly due to electrostatic interactions rather than van der Waals force [32].

The scope of most of these previous studies is limited to the experimental determination of interface bonding properties and their impact on the tensile behavior of composites. Since the main reaction products in a cementitious matrix and an alkali-activated matrix are not the same, the influence of reaction product chemistry on the interface bonding properties of PVA fiber, as well as its interaction mechanism with the AASF system, is worth to be studied in more depth. This can help understand the microscale interface bonding properties and mechanisms, which are of primary importance for the development of PVA fiber-reinforced alkali-activated composites (such as SHGC). In the existing studies, however, the influence of the reaction product chemistry on the interface bonding properties are usually neglected. Furthermore, studies on the interfacial transition zone (ITZ) between the PVA fiber and AASF matrix have been rarely reported.

The goal of this experimental study is to characterize the interface bonding properties of PVA fiber in AASF matrices and to further clarify the effects of PVA fiber on the reaction products chemistry in the PVA fiber/matrix ITZ in AASF matrices. To this end, the chemical bonding energy G_d, initial frictional bond τ_0, and slip-hardening coefficient of PVA fiber to the AASF matrix were systematically investigated using single-fiber pullout tests. The influence of PVA fiber on the microstructure of the ITZ and the chemical composition of the reaction products within the ITZ were characterized using multiple techniques. Based on the experimental results, the relationship between G_d and the chemical composition of the reaction products was further explored. The origin of the initial frictional bond and slip-hardening behavior of PVA fiber in AASF pastes were also discussed.

2. Materials and methods

2.1 Materials

The solid precursors were ground granulated blast furnace slag and Class F fly ash produced locally in the Netherlands. The physical properties, chemical compositions, mineralogical composition, and reactivity of both raw materials have been reported in our previous studies [17, 25]. The polyvinyl alcohol (PVA) fiber (RECS 15, Kuraray) with 1.2% oiling treatment on the surface was used. The chemical structure of the PVA fiber is shown in Figure 1. The PVA polymer is primarily composed of the vinyl group (C-OH) with a minor content of the acetate group (C-OCOCH3). According to the supplier, the acetate group is introduced by the synthesis process, although it is the vinyl group that determines the surface property of the fiber.

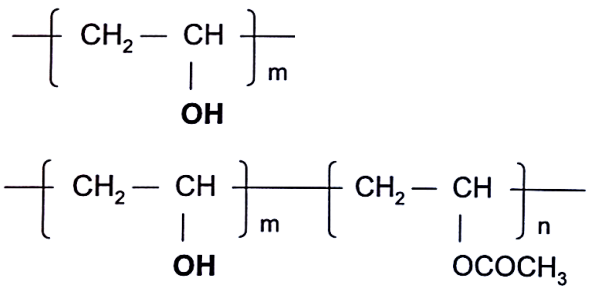

Figure 1 Structure of PVA polymer according to the fiber supplier [33]

The physical and mechanical properties of PVA fiber are presented in Table 1. A filament-type PVA fiber with a diameter of 40 μm was adopted for the characterization of the mechanical properties of the fiber/matrix interface. The study of the ITZ, whereas, adopted PVA fiber with a diameter of 300 μm in order to facilitate the characterization of ITZ by means of ESEM and EDX. The alkaline activator was a sodium-based silicate solution prepared by dissolving NaOH pellets (analytical grade, purity≥98%) and sodium silicate (Na_2O: 8.25 wt.%, SiO_2: 27.50 wt.%) in distilled water. The activator solution was cooled down to room temperature before mixture preparation.

Table 1 Physical and mechanical properties of PVA fiber

Fiber	Diameter (μm)	Density (g/cm^3)	Length (mm)	Strength (MPa)	Elastic modulus (GPa)
PVA	40, 300	1.30	filament	1640	41.1

2.2 Mixture design and preparation

The mixture design originates from AASF pastes that exhibit a good combination of fresh properties and mechanical properties [18]. Since the microstructure and reaction product of AASF pastes is significantly influenced by the contents of Si from the activator [13, 17, 34], the silicate modulus M_s (M_s being the SiO_2/Na_2O molar ratios) of the activator was selected as the main variables in this study. The mixture design of AASF paste matrices is shown in Table 2, in which the binder composition with different activator silicate modulus M_s (0 to 1.5) are given. The AASF matrices were named M0 to M1.5 accordingly. In each mixture, the w/b ratio and Na_2O content (in activator with respect to total binder mass) were kept constant to be 0.32 and 4%, respectively. The w/b ratio was chosen in a way that adequate workability for all paste mixtures was maintained.

Table 2 Mixture proportions of alkali-activated slag/fly ash matrices

Mixture	Solid precursor (wt.%)		Alkaline activator (wt.%)			
	Slag	Fly ash	Water	Na_2O	SiO_2	Silicate Modulus M_s
M0	50	50	32	4.0	0	0
M0.5					1.94	0.50
M0.8					3.10	0.80
M1.0					3.88	1.00
M1.2					4.65	1.20
M1.5					5.82	1.50

2.3 Determination of interface bonding properties

The interface bonding properties of PVA fiber AASF matrices were tested experimentally by single-fiber pullout tests with the set-up following Redon et al. [28]. The set-up is shown in Figure 2 (a). A mold equipped with two-layer polyethylene (PE) bricks developed by Katz and Li [35] was used. The PVA fiber was cut, aligned, and fixed onto the PE brick using double-sided tape. The fresh AASF paste was then poured into the mould around the fibers. The specimens were put on a vibration table to remove entrapped air before sealing them with plastic wrap. After 24 hours, the specimens were demolded and transferred to a climate room (20°C and 95% RH) until 28 days. At 28 days, the hardened specimens were cut into very thin sliced samples using a low-speed saw (Minitom, Struers). As shown in Figure 2 (b), the cutting leaves the fiber on one side of the sample. The thickness of the sample, i.e., the embedded length (L_e) of PVA fiber, was approximately 1 mm, which was short enough to avoid fiber rupture during the fiber pullout process.

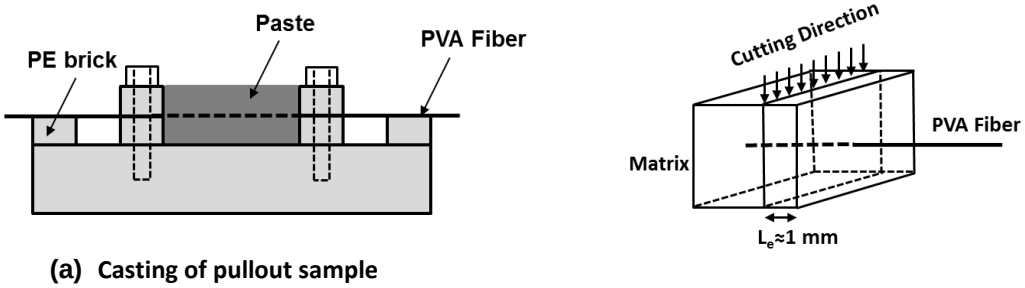

Figure 2 Pullout sample preparation methods: (a) casting and (b) precise cutting [25].

For the single-fiber pullout tests, a micro tension-compression testing device (Kammrath & Weiss) was used as shown in Figure 3 (a). The schematic pullout test set-up is shown in Figure 3 (b). The surface of the thin-sliced sample and the free end of the PVA fibers were glued to two small metal blocks. The fiber was then aligned vertically to the matrix surface to avoid the influence of matrix spalling on the testing result. A hex nut was applied in between the cut surface and the metal block to avoid gluing the fiber ends. Then, the two metal blocks with the pullout sample were carefully mounted onto the testing device and were further fixed to an actuator and a load cell. Notably, a fiber segment

with a length of approximately 1 mm was kept free of loading between the actuator and the pullout sample. A 10 lb (44.48 N) load cell was used to measure the pullout load with an accuracy of 0.1%. The pullout tests were conducted using displacement control with a constant displacement rate of 0.01 mm/s. At least 20 tests were conducted for each fiber/matrix combination.

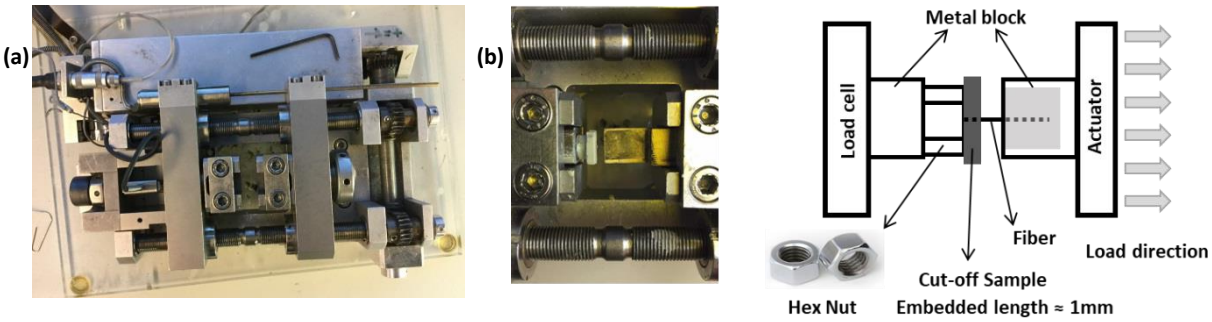

Figure 3 Single-fiber pullout test: (a) micro tension-compression device, (b) schematic tests set-up [25].

To quantitatively determine the interface properties, the chemical bonding energy G_d, initial frictional bond τ_0, and slip-hardening coefficient β were derived from the single fiber pullout curves (see Figure 4) with Equations (1) to (3). All these equations were derived from a fiber debonding/pullout model by Lin et al. [36]. In formula form:

$$G_d = \frac{2(P_a - P_b)^2}{\pi^2 E_f {d_f}^3} \quad (1)$$

$$\tau_0 = \frac{P_b}{\pi d_f L_e} \quad (2)$$

$$\beta = \frac{d_f}{L_e}\left(\frac{(\Delta P/\Delta S\,|\Delta S \to 0)}{\pi \tau_0 d_f} + 1\right) \quad (3)$$

where E_f, d_f, and L_e are the elastic modulus [GPa], diameter [mm], and embedded length [mm] of PVA fiber, respectively. $\Delta P/\Delta S$ is the initial slope of the pullout load P [N] vs displacement S [mm]. P_a is the load at the moment when the fiber is fully debonded (debonded length L_d = embedded length L_e) and P_b is the load when the fiber starts to slip.

2.4 Microstructural characterizations

The microstructure and the chemical compositions of reaction products in AASF bulk matrices and the (possible) ITZ around PVA fiber were characterized using environmental scanning electron microscopy (ESEM) and energy dispersive X-ray (EDX) analysis. In this study, the area of interest extends to as far as 30 μm away from the fiber. Such range is considered appropriate to study the influence of PVA fiber on the reaction product formation at the fiber/matrix interface (see also [37]). Mixtures including M0 to M1.5 were used to characterize the reaction product composition in AASF bulk matrices. Only the M1.0 sample as a representative was studied to determine the distribution of

element/reaction products near the PVA fiber. All samples were prepared following the method for single fiber pullout tests as described in Section 2.3.

Before the ESEM/EDX tests, the chemical reaction in hardening pastes was stopped by the solvent exchange method using isopropanol. After vacuum drying, the samples were impregnated using low-viscosity epoxy resin. After the hardening of the epoxy resin, the samples were polished until reaching a surface roughness of 0.25 µm. Backscattered electron (BSE) images and secondary electron (SE) images were taken at an accelerating voltage of 15 kV and 5 kV, respectively. The polished samples were coated with carbon and then the EDX measurements were conducted at an accelerating voltage of 15 kV in high vacuum mode.

Furthermore, ESEM/EDX-based spectral imaging (SI) was performed to study the chemical compositions of the reaction products. The points for EDX spot analysis were carefully selected within the binder region, keeping sufficient distance from the unreacted slag and fly ash particles [38]. In each EDX measurement, corrections on the characteristic X-ray intensity were made by taking into account the atomic number, absorption, and fluorescence excitation (ZAF) effect. These corrections convert apparent concentrations (raw intensities) into corrected concentrations to eliminate inter-element matrix effects.

Finally, automated phase mapping was used to study the phases formed in AASF pastes under the influence of PVA fiber. For this purpose, the COMPASS™ as a built-in function in the Pathfinder software (Thermofisher Scientific) was applied. The phase mapping was based on the analysis of spectral imaging (SI) data using principal component analysis (PCA). With a multivariate statistical approach, COMPASS could analyze the spectrum at each pixel location and groups the pixels with similar spectra together into principal components [39]. These principal component maps were translated into phase maps using the same types of intensity threshold algorithms used for traditional element-based phase mapping. The phase spectrum was thus the summation of the spectra from each pixel within the phase [39, 40]. The final results were a list of chemically unique phase spectra and phase maps. In this way, the hidden phases could be also revealed, regardless of the inevitable intermixing of the phases and the noise signals from unreacted precursor particles [41]. For one automated phase mapping analysis, at least 300 frames of EDX element mapping were taken on the selected area covering the PVA fiber, the ITZ, and the matrix. The presence of the phases was further examined by the density plots using the channel intensity correlations (net counts) from each pixel of the EDX phase mapping.

3. Results and discussions

3.1 PVA fiber/matrix interface bonding properties characterization

3.1.1 Single-fiber pullout behavior

The single-fiber pullout behavior, i.e., the load-displacement relationship of PVA fibers embedded in the AASF matrix, is shown in Figure 4 (a). The PVA fiber debonding and pullout behavior in the AASF matrix is similar to that of PVA fiber in the cementitious matrix [28, 42]. As illustrated in Figure 4 (b), the general profile of a single-fiber pullout curve can be decomposed into three main regimes [28]: (1) the stable debonding stage in which the load increases up to P_a until the moment when the debonded length equals the embedded length of the fiber, (2) the slippage stage in which the fiber starts to slide from load P_b and the pullout is resisted by frictional forces only, and finally (3) the slip-hardening stage in which the friction force increases linearly with increasing pullout distance up to the maximum load P_{max} before the fiber ruptures. The increasing pullout resistance is referred to as the slip-hardening effect and is characterized by the slip-hardening coefficient β (β>0) [43].

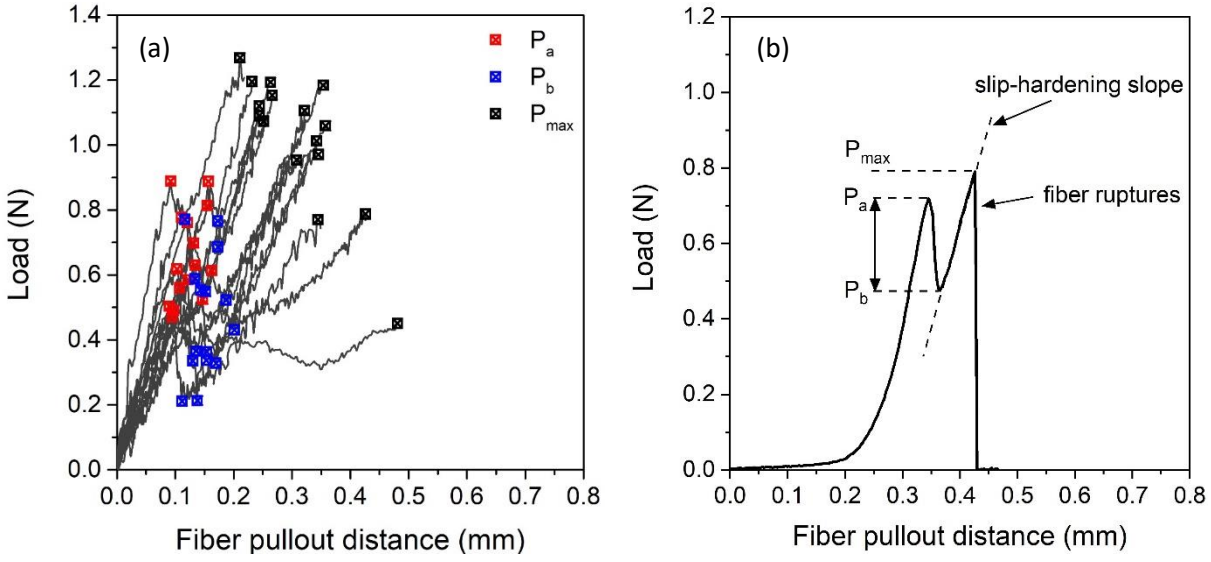

Figure 4 (a) Representative pullout curve of PVA fiber in AASF matrix; and (b) schematic illustration of fiber pullout process.

The results of all interface bonding properties including chemical bonding energy G_d, initial frictional bond τ_0, and slip-hardening coefficient β are given in Table 3. Their standard deviations (STDs) generally fall between 25% to 40% of the mean values. The clustering of the data around the mean value thereby implies the trend in the data set could be determined using the mean values.

Table 3 PVA fiber/matrix interface bonding properties

Mixture	Chemical bonding energy G_d (J/m^2)	Initial frictional bond τ_0 (MPa)	Slip-hardening coefficient β
M0	4.61±1.21	2.29±0.56	0.34±0.05
M0.5	6.15±1.49	4.09±1.14	0.43±0.08
M0.8	4.92±1.27	3.22±0.81	0.47±0.13
M1.0	3.74±1.31	3.41±0.84	0.44±0.10
M1.2	3.29±1.34	3.21±0.82	0.40±0.08
M1.5	2.62±0.88	2.96±0.97	0.35±0.09

3.1.2 Chemical bonding energy G_d

Most previous studies assume that the debonding process in the fiber pullout test is a tunnel crack propagation and the pullout of the fiber is thereby resisted by the debonding fracture energy of the tunnel-shaped crack [36]. This fracture energy is also known as the chemical bonding energy G_d and can be calculated by Equations (1) [28]. The G_d of PVA in AASF matrices is presented in Figure 5, in which the average values of G_d versus the activator silicate modulus (M_s) show a clear trend. The values of G_d vary from 2.6 to 6.2 J/m^2 with the M_s ranging from 0 to 1.5. Knowing that the G_d normally ranges from 1 to 2 J/m^2 [29] in conventional strain-hardening cementitious composite (SHCC) and from 0.5 to 1.5 J/m^2 in high-volume fly ash SHCC [30], the chemical bonding of PVA fiber (with 1.2% oiling) in AASF matrices is significantly stronger than those reported in the above cementitious systems. In fact, the average values of G_d in SHGC matrices are generally 1.5 to 2.5 times higher than those in conventional SHCC [27, 29, 30]. Notably, the SHCC matrices in these studies have a limited amount of fine quartz sand with a maximum particle size of 250 μm. However, due to the limited sand content (lower than 30 wt.%) and fineness (average particle size 110 μm), a reasonable comparison of the interface bonding properties between two systems can be made. Furthermore, with increasing M_s, G_d first increases, peaks at M_s of 0.5, and then gradually decreases. This trend is somehow well correlated with the chemical composition change of the reaction product with increasing M_s. Further discussions are given later in Section 3.3.1.

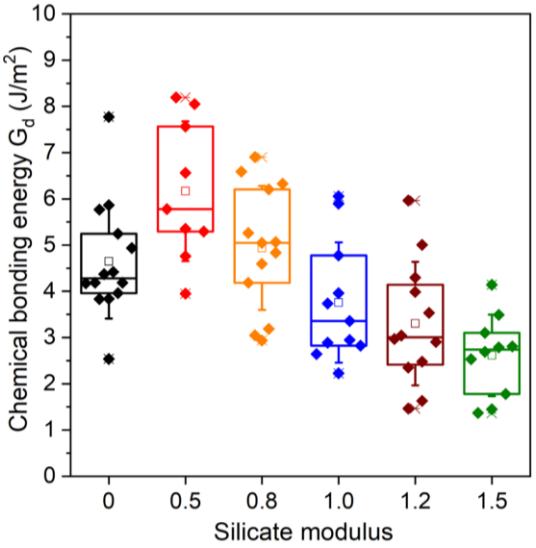

Figure 5 Box plot of chemical bonding energy (G_d) of PVA fiber in AASF matrices with different activator silicate modulus. The box plot illustrates the median value (-), the mean (□), the values at 25% and 75% (box edges), and the standard deviation (Whiskers).

3.1.3 Initial frictional bond τ_0 and slip-hardening coefficient β

The initial friction bond τ_0 for AASF mixtures with M_s from 0 to 1.5 As shown in Figure 6 (a). Despite the relatively large STDs, the mean value of τ_0 follows a somewhat similar trend when comparing to G_d. It also reaches a maximum value at M_s 0.5 and then in general decreases with increasing M_s. Notably, the mean τ_0 is found to be about 2 to 3 times higher than those in cementitious systems [27, 30]. The slip-hardening coefficients β of the AASF mixtures are shown in Figure 6 (b). The mean values of β are in a range of 0.26 to 0.42, which are much lower than those found in conventional SHCC (1.15) [29] and high-volume fly ash-based SHCC (0.58-0.63) [44]. No clear trend of β could be identified with increasing M_s.

The above findings, in line with several previous studies of SHGC [23-25], thus demonstrate significant differences in interface bonding properties in SHGC. Further discussions on the origin of the frictional bond and the mechanism of slip-hardening are given in Section 3.3.3.

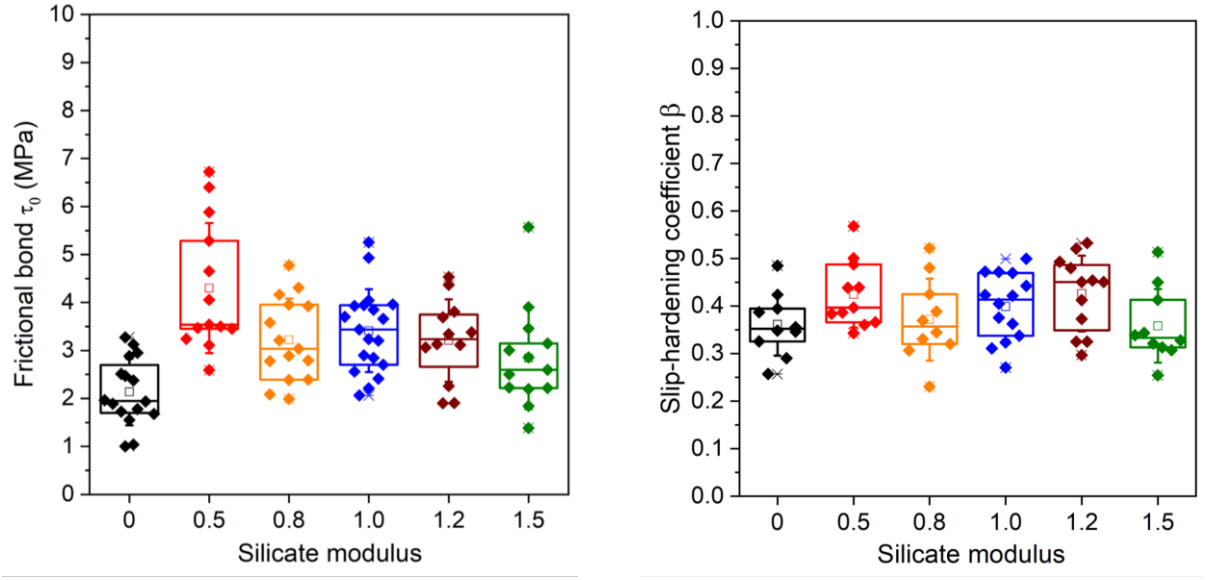

Figure 6 Box plot of (a) initial frictional bond (τ_0) and (b) slip-hardening coefficient β of PVA fiber in AASF matrices with different activator silicate modulus. The box plot illustrates the median value (-), the mean (□), the values at 25% and 75% (box edges), and the standard deviation (Whiskers).

3.2 Microstructural characterization of ITZ

3.2.1 Morphology of PVA fiber/matrix interface

The morphology of the PVA fiber/matrix interface was firstly observed using backscattered electron imaging on polished sections. Figure 7 (a) and (b) show typical BSE micrographs of the cross-section of both the PVA fiber and the ITZ in AASF (M1.0). The grey level contrast in both BSE micrographs distinguishes among different constituents, i.e., the PVA fiber, reaction products, the remnant slag and fly ash particles, as well as the micro-cracks and pores.

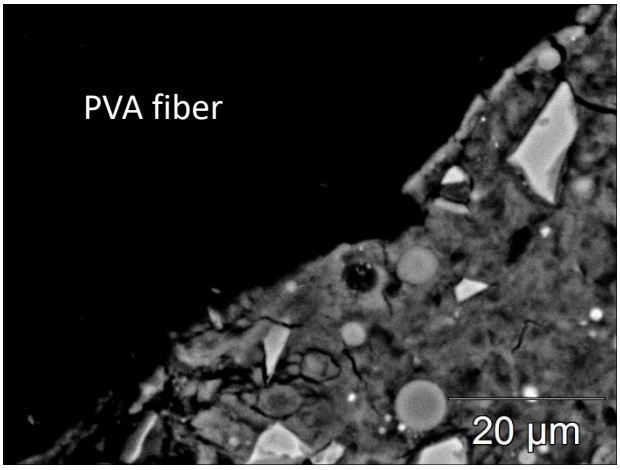

(a) the ITZ of PVA fiber in AASF matrix M1.0

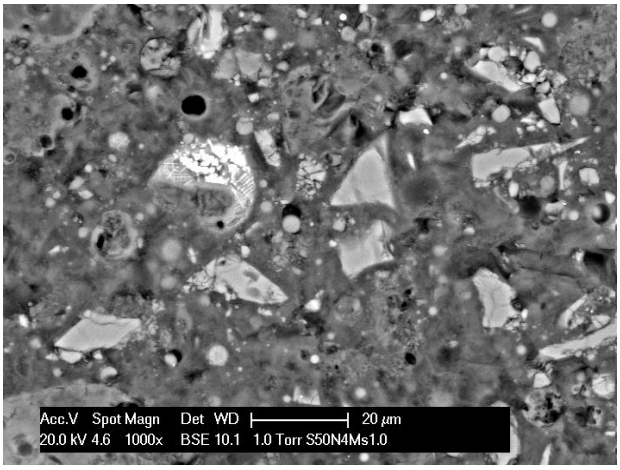

(b) the AASF matrix M1.0

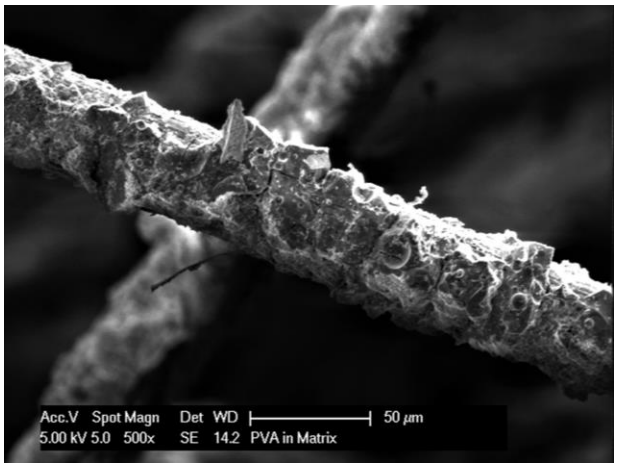

(c) PVA fiber surface after single-fiber pullout

Figure 7 Comparison of typical SEM micrographs of (a) the ITZ of the AASF M1.0 at 28 days and (b) AASF matrix M1.0 at 28 days.

The presence of a 300 μm PVA fiber in the matrix could disturb the packing of slag particles. This is known as the wall effect, which could increase the local liquid-to-solid ratio near the PVA fiber [45]. However, the ITZ around the 300 μm PVA fiber in the 28-day bulk AASF matrix was found to be not significantly more porous compared to the bulk matrix. This observation is consistent with previous studies on the ITZ around the fine sand particle (300 μm) in alkali-activated slag (AAS) mortar, which was found to be dense with very low porosity [46, 47]. As a result, Figure 7 thus suggests that the wall effect around a 300 μm PVA fiber in the AASF matrix is not significant. Based on this evidence, it is conceivable that the wall effect of a 40 μm PVA fiber in the AASF matrix is even less significant.

Furthermore, the reaction products in the ITZ appeared to be firmly attached to the surface of the PVA fiber. This observation is also confirmed by the SE micrograph in Figure 7 (c) of the pulled-out fiber after the single-fiber pullout tests. However, unlike the finding of the portlandite phase formed around PVA fiber in the cementitious system [48], no newly-formed crystalline phases (with distinct morphological characteristics) could be observed.

3.2.2 Phase mapping based on the chemical composition

To further assess the reaction product formed in the ITZ, the automated phase mapping based on the chemical composition of different phases was applied using a principal component analysis (PCA) approach. The results of PVA fiber in the M1.0 matrix are illustrated in Figure 8. The unreacted slag particles, unreacted fly ash particles, and PVA fiber can be clearly identified. Furthermore, phase mapping also helps to identify at least three types of chemically distinct reaction products. Their representative EDX spectra are given in Figure 9 and the chemical compositions of these phases (atomic ratios) are given in Table 3.4. Based on their chemical compositions, the three phases are labeled as (1) high-Ca C-(N-)A-S-H, a C-(N-)A-S-H gel with very high Ca content; (2) C-(N-)A-S-H + Ht, a C-(N-)A-S-H gel intermixed with Mg-rich hydrotalcite (Ht), and (3) a C-(N-)A-S-H gel, the major reaction product formed in the matrix. The latter two phases are commonly found in AAS and AASF with high slag content (>50 wt. %) [13].

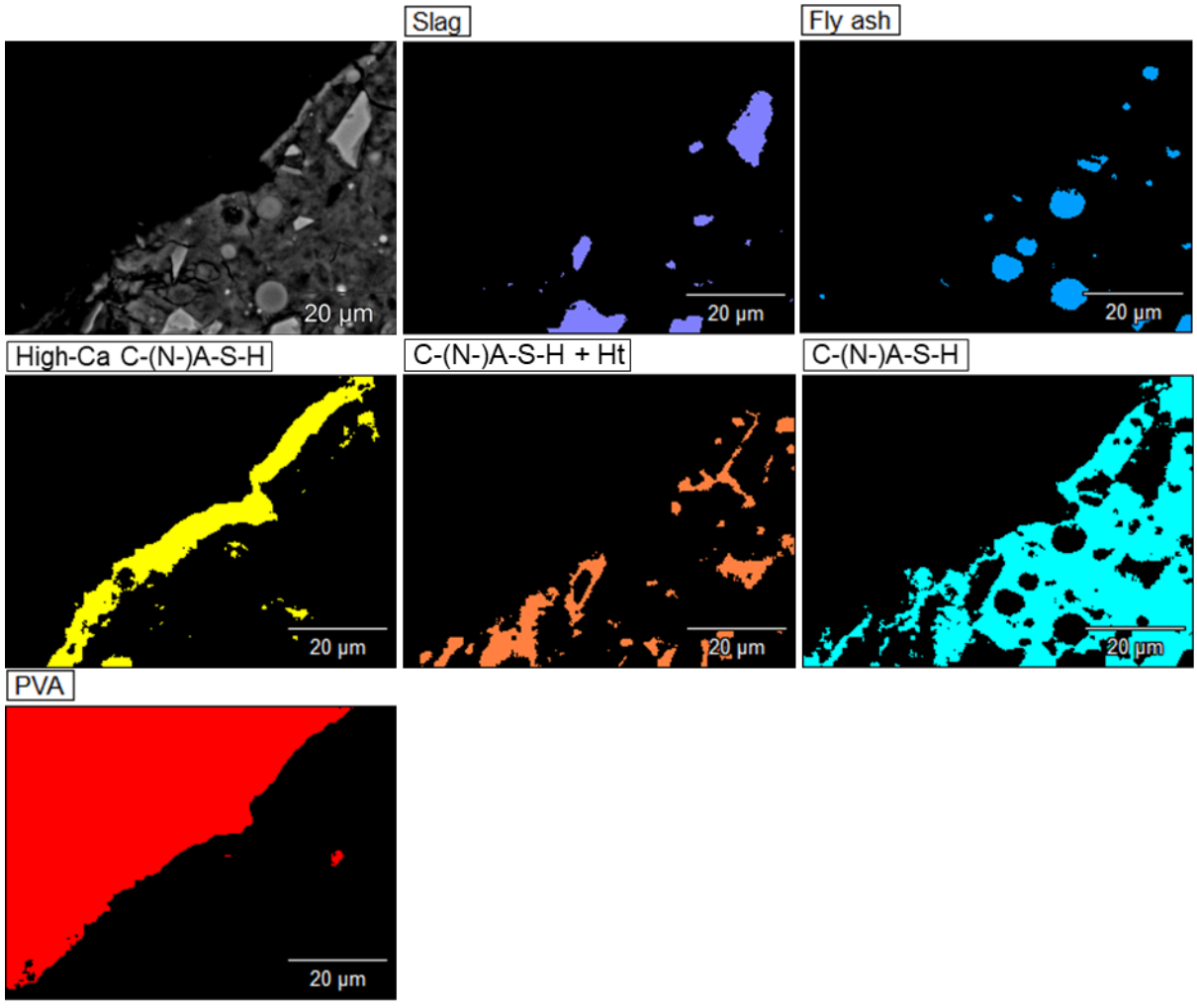

Figure 8 Phases mapping using principal component analysis based on the chemical composition of reaction products (in atomic %) in the ITZ of M1.0

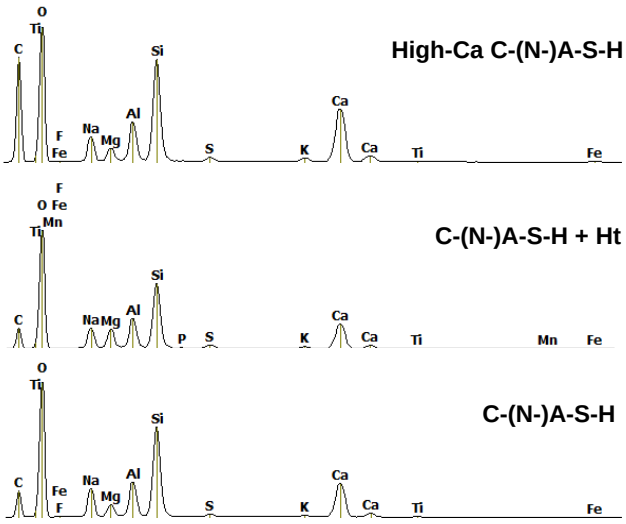

Figure 9 EDX spectra for three C-(N-)A-S-H phases identified by automated COMPASS phases mapping: High-Ca C-(N-)A-S-H, C-(N-)A-S-H + Ht, and C-(N-)A-S-H phases

Table 3.4 Atomic ratios of the reaction products determined by EDX spot analysis

Reaction product	Ca/Si	Ca/(Si+Al)	Al/Si	Mg/Ca	Mg/Si
High-Ca C-(N-)A-S-H	1.82±0.53	1.44±0.30	0.34±0.06	0.12±0.03	0.13±0.03
C-(N-)A-S-H + Ht	0.61±0.03	0.43±0.05	0.42±0.05	0.50±0.11	0.31±0.11
C-(N-)A-S-H	0.61±0.04	0.43±0.05	0.40±0.05	0.24±0.11	0.15±0.11

Note: Hydrotalcite (Ht) phases as secondary reaction products are intermixed with the main reaction product C-(N-)A-S-H gel, although the amount of hydrotalcite differs according to the region for EDX testing as can be reflected by the Mg/Ca and Mg/Si ratio.

High-Ca C-(N-)A-S-H phase

The most important finding is the Ca-rich reaction product formed in the ITZ, namely the high-Ca C-(N-)A-S-H (Table 3.4). The location of this phase matches perfectly the location of the Ca-rich rim around PVA fiber in the EDX element mapping reported in our previous study [32]. Further EDX spot analysis in the area of the Ca-rich reaction product and the rest areas in the matrix are presented in a CaO-SiO_2-Al_2O_3 ternary diagram in Figure 10. The result shows that the high-Ca C-(N-)A-S-H phase has a significantly higher Ca/Si (1.82) and Ca/(Si+Al) ratio (1.44) than both C-(N-)A-S-H and C-(N-)A-S-H+Ht phases (see also Table 3.4,). On the other hand, the high-Ca C-(N-)A-S-H phase has at least a similar Al/Si ratio as the reaction products formed elsewhere. In fact, despite its high Ca content, Figure 9 shows the high-Ca C-(N-)A-S-H phase has the characteristic EDX spectrum of C-(N-)A-S-H gel, which has been confirmed by our previous study as the main reaction product formed in identical AASF systems [18]. All the above evidence indicates the high-Ca C-(N-)A-S-H formed near the PVA fiber surface is a kind of C-(N-)A-S-H gel with a high Ca/Si ratio and Ca/(Si+Al) ratio.

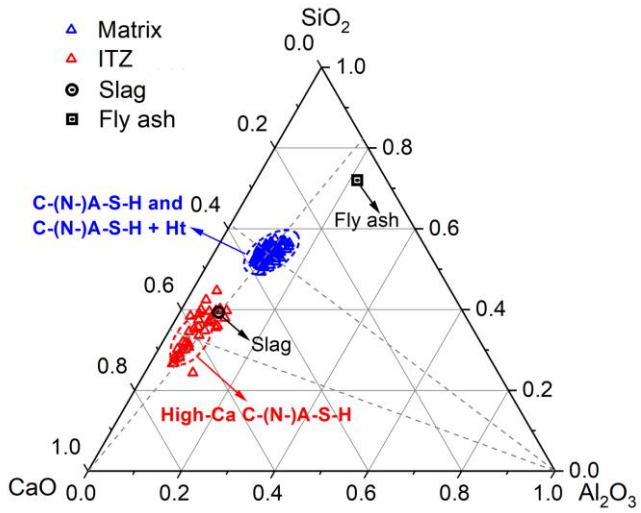

Figure 10 Ternary diagram of CaO-SiO_2-Al_2O_3 of EDX spot analysis for reaction product in the matrix and the Ca-rich region in the ITZ

The formation of the high-Ca C-(N-)A-S-H is due to the hydroxyl group on the PVA fiber surface. Our previous study within identical AASF matrices using MD simulation indicates the polarity of the PVA molecule induced by the hydroxyl functional group and its interaction with C-(N-)A-S-H gel presents a high affinity of Ca and Na cations to the PVA molecule, leading to a higher coordination number of Ca to O_{PVA} in comparison to Si and Al [32]. At an early age, the strong polarity induced by the hydroxyl group effectively attracts the free-moving Ca^{2+} cation in the pore solution to accumulate near the PVA fiber surface. This effect leads to the formation of Ca-rich C-(N-)A-S-H gel that later will have considerable influence on the chemical bonding energy of PVA fiber in the AASF matrix.

Interestingly, this finding is somewhat different than what has been reported in cementitious systems. There, the Ca-rich reaction product around the PVA fiber is a layer of crystalline portlandite (CH) [30, 48, 49] and it plays a dominant role in determining the interface bonding properties in PVA-based SHCC [50]. In the AASF system, however, the formation of CH as a crystalline phase is highly unlikely because CH has a much higher solubility product K_{sp} than C-(N-)A-S-H gel [51]. In this case, the formation of the amorphous C-(N-)A-S-H gel is more preferential as predicted by thermodynamics modeling [52, 53]. In fact, the main reaction products of sodium silicate-based AASF are reported to be amorphous [13, 34, 54] and seldom have new crystalline phases except for hydrotalcite has been reported. The above evidence thus precludes the possibility that the Ca-rich reaction product is due to the intermixing of C-(N-)A-S-H gel with CH.

It is also worth noting that the reaction product around aggregate particles in previous studies on AAS mortar has a lower Ca/Si ratio than that in the bulk matrix due to the “wall effect” [47]. The higher Ca/Si ratio of the reaction product near the PVA fiber thus indicates that the physical “wall effect” is not dominating in this case. Instead, the chemical characteristics of the PVA fiber surface could play a more significant role in the formation of Ca-rich reaction products. This could also be the reason for

the differences between the chemical bonding energy of PVA fiber in AAMs systems and cementitious systems [23-25]. Further discussions are given in Section 3.3.2.

C-(N-)A-S-H and C-(N-)A-S-H+Ht phase

The phase mapping also identified two types of C-(N-)A-S-H phase, viz., C-(N-)A-S-H and C-(N-)A-S-H+Ht (see Table 3.4). The presence of these two phases could not be shown using the CaO-SiO_2-Al_2O_3 ternary diagram, because their Ca, Si, and Al composition are rather similar. However, they can be distinguished by their different Mg composition (Table 4.3) using the CaO-Al_2O_3-MgO ternary diagram in Figure 11. It is evident that the C-(N-)A-S-H+Ht phase has a higher Mg content than the C-(N-)A-S-H phase.

As shown in Figure 8, the C-(N-)A-S-H+Ht phase is distributed majorly around the unreacted slag particles. This region matches the so-called “dark rim” around the remnant slag particles, which has been detected in previous research on AAS and AASF [53-57] due to the in-situ reaction between the outer layer of GGBFS and alkali [58, 59]. The Mg ions, due to their low mobility, cannot significantly migrate away from the original slag grain [60]. This is also the reason for the formation of the “dark rim”. Since hydrotalcite (Ht) is the only possible reaction product containing Mg, the higher Mg/Si and Mg/Ca ratios in Table 3.4 thus suggest that the reaction products around the slag particles are most probably a composite phase of C-(N-)A-S-H and hydrotalcite (C-(N-)A-S-H+Ht) [59, 61]. Unlike the C-(N-)A-S-H+Ht phase, the C-(N-)A-S-H phase is distributed quite homogeneously in the matrix. It is also the most abundant with the largest area coverage in the phase mapping (Figure 8).

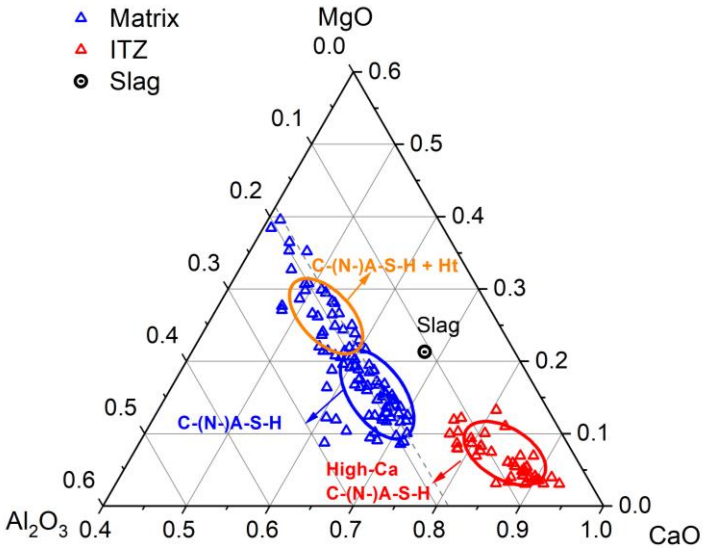

Figure 11 CaO-Al_2O_3-MgO ternary diagram of EDX spot analysis in the ITZ

Unfortunately, the EDX element/phase mapping cannot distinguish separately the hydrotalcite and the C-(N-)A-S-H phase. Hydrotalcite is a layered double hydroxide (LDH). Its host brucite-like Mg-Al layers have a strong positive charge [62]. As a result, the hydrotalcite layers are strongly attracted to the

negatively charged C-(N-)A-S-H layers during the alkali-activation reaction. This affinity thereby leads to a highly intermixed hydrotalcite and C-(N-)A-S-H gel at the nanoscale [58]. For a clear separation of intermixed phases at this scale, most X-ray based analysis techniques have reached their resolution limits. As a result, the hydrotalcite phase was rarely studied individually in AASF pastes.

3.2.3 Density plots of phases based on EDX element mapping

The presence of the phases determined by the automated phase mapping is further examined by the density plots using the channel intensity correlations between (1) Ca+Al+Si versus Mg and (2) Ca+Al+Si+Mg versus Na. The channel intensities used here are the net counts from each pixel of the EDX phase mapping. They were extracted from the spectra imaging (SI) data from the phase mapping results in Figure 8. The density plots of the abovementioned two correlations were created following Van Hoek et al. [63] and Nedeljković et al. [54]. The Ca+Al+Si versus Mg density plots in Figure 12 (a) help to distinguish the remnant slag and fly ash particles, and the PVA fiber from the reaction products. The Ca+Al+Si+Mg versus Na density plots in Figure 12 (b) help to better illustrate the differences between the reaction products. In all density plots, the statistically distinct phases could then be distinguished by their different positions in the data cluster, with the abundance of the phases reflected by the different colors.

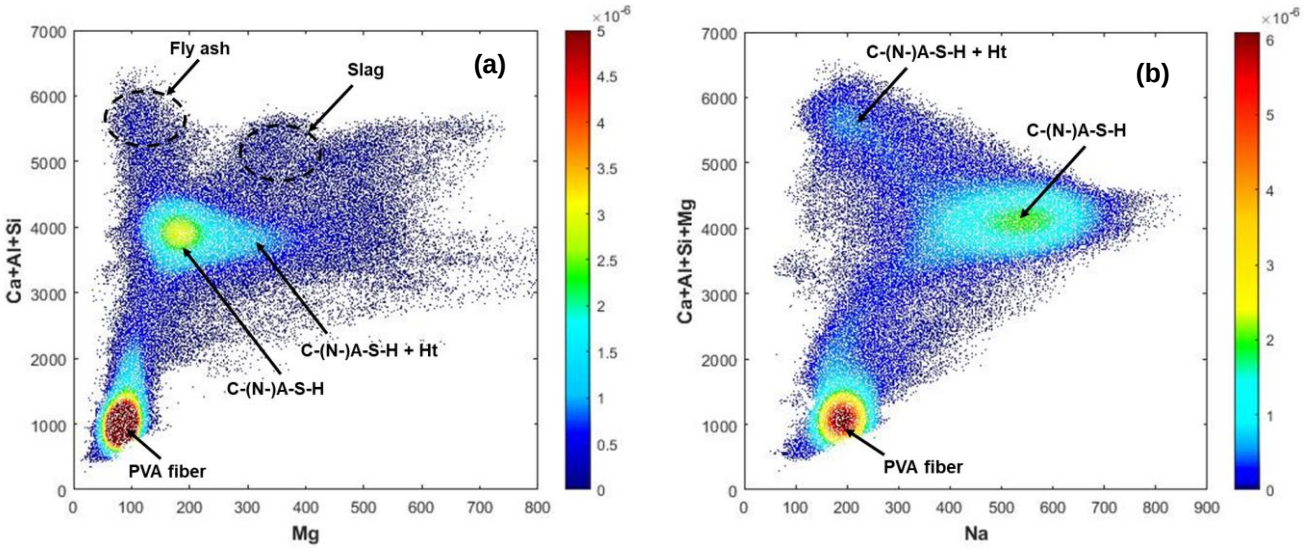

Figure 12 Density plot of channel intensities Ca+Al+Si versus Mg, and density plot of channel intensities Ca+Al+Si+Mg versus Na.

The clusters of PVA in all density plots show the highest abundance in red color. This is in line with the phase mapping in Figure 8 where the PVA fiber occupies almost half of the areas. There are no evident clusters for remnant slag and fly ash particles, indicating their limited content in the ITZ. The positions of clusters for slag and fly ash particles have been marked in Figure 12 (a) and (b) with black dotted circles. The C-(N-)A-S-H and C-(N-)A-S-H+Ht phases, as the main reaction products, could be distinguished according to their different Mg content. In comparison to C-(N-)A-S-H, C-(N-)A-S-H+Ht

phase is more abundant in all density plots. These results coincide well with the ones from the phase mapping in Figure 8, in which C-(N-)A-S-H among all reaction products occupies the largest area. No sharp boundaries are observed between these two phases. Similar findings were found by Nedeljković et al. [54] using Phase Recognition and Characterization (PARC), the reaction products, namely Ca-Na-Al-Si-H gel and Ca-Mg-Na-Al-Si-H gel, which correspond to the C-(N-)A-S-H and C-(N-)A-S-H+Ht, respectively [54].

3.3 General discussions

3.3.1 Debonding scenarios between PVA fiber and AASF matrix

It is generally assumed that the debonding would happen along the weakest link among constituents in the fiber-reinforced composite, for example, along the fiber/matrix interface [64]. However, considering the strong adhesion between PVA fiber and AASF matrix (Section 3.1.2), the bond failure scenarios could be different. A schematic representation of the possible bond failure scenarios is illustrated in Figure 13, which depicts the debonded surfaces at the end of the fiber debonding process, i.e., the starting point of the slippage phase. This is also the moment when the pullout load drops from P_a to P_b in Figure 4 (b). With the completion of the debonding process, three possible debonding scenarios can be considered:

- Scenario I: the debonding due to the adhesive failure at the interface (PVA-matrix).
- Scenario II: the debonding due to the cohesive failure of the matrix in the ITZ (matrix-matrix).
- Scenario III: the debonding due to the combined adhesive-cohesive failure [65].

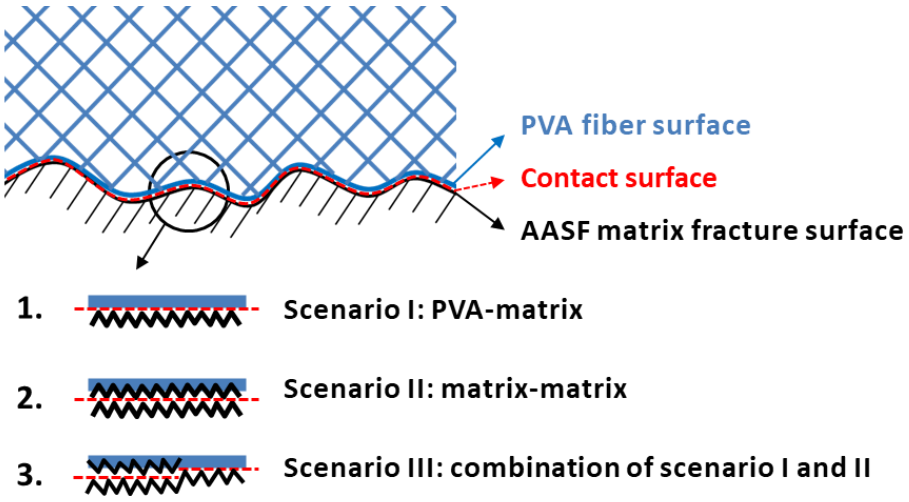

Figure 13 Schematic representation of the bond failure scenarios.

The debonding scenario I normally holds for hydrophobic polymeric fiber, which have negligible adhesion with the reaction product in the matrix [42, 66, 67]. During pullout, the tunnel crack propagates exactly along the fiber surface. The adhesive failure at the interface determines that the

later friction will be between the fiber surface and the matrix [68]. This is also the reason why the friction between the hydrophobic fibers and the matrix could be substantially improved by increasing the surface roughness of the fibers [66, 69, 70]. In contrast, debonding according to scenario II occurs normally when a hydrophilic fiber strongly adheres to the matrix. Under such circumstances, the adhesion between fiber and matrix is stronger than the cohesion in the matrix. As a result, the tunnel crack tends to propagate in the matrix near the PVA fiber leading to the cohesive failure of the matrix in the ITZ. Finally, debonding scenario III happens when the adhesion between fiber and matrix is about equal to the cohesion in the matrix. The tortuous tunnel crack propagates partially along the fiber surface but also in the matrix, which leads to an adhesive-cohesive failure in the ITZ [29, 71].

In this study, even after the pullout, the surface of PVA fiber appears to be almost fully covered with matrix residue (see also Figure 7 (c)). Considering the very high G_d of PVA fiber in AASF matrices (2 to 3 times higher than that in cementitious materials), the debonding is most probably scenario III, but dominated by scenario II [72, 73].

3.3.2 Chemical bonding energy G_d and chemical composition of C-(N-)A-S-H gel

The main reaction product in AASF pastes was characterized to be C-(N)-A-S-H gel (Section 3.2.2). By changing the activator M_s, the availability of silica species was effectively altered and thereby changed the global reaction and chemical nature of the reaction products [74-76]. Such effects lead to the formation of C-(N-)A-S-H gel with various Ca/Si and Ca/(Si+Al) ratios. A strong linear relationship was also identified between chemical bonding energy G_d and the Ca/Si and Ca/(Si+Al) ratios of the C-(N-)A-S-H gel in AASF pastes shown in Figure 14. This implies that the G_d of PVA fiber in AASF pastes is also strongly governed by the chemical composition of C-(N-)A-S-H gel.

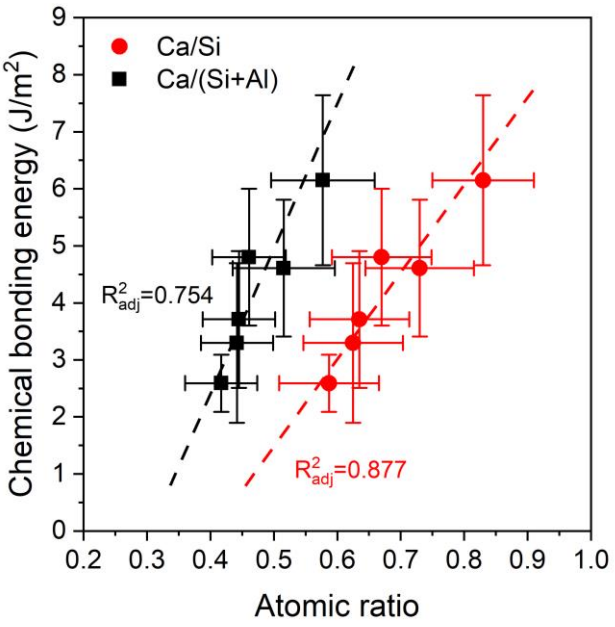

Figure 14 Correlation of chemical bonding energy G_d as a function of Ca/Si and Ca/(Si+Al) ratios of C-(N-

)A-S-H gel in AASF pastes.

Based on the experimental results and discussions in this study, the reason for the strong correlations between the G_d and the Ca/Si and Ca/(Si+Al) ratios of the C-(N-)A-S-H gel could be due to both the adhesion between fiber and matrix and the cohesion of the matrix in the ITZ (scenario III).

First of all, the hydroxyl group (-OH) on the surface of PVA fiber has a strong polarity due to the high electronegativity of the oxygen atom. It thus serves as a favorable oxygen site provider for the formation of electrostatic interactions. Similar to C-S-H gel, C-(N-)A-S-H gel with high Ca/Si or Ca/(Si+Al) ratios present a high negative surface charge density [77]. Under such circumstances, the formation of the electrostatic $O_{C\text{-}(N\text{-})A\text{-}S\text{-}H}$-Ca-$O_{PVA}$ bonds is highly feasible [78, 79]. In fact, our previous studies on PVA fiber in identical AASF matrices have confirmed that the chemical bonding (adhesion) between PVA and C-(N-)A-S-H gel is mainly due to such electrostatic interactions between the hydroxyl group (-OH) in PVA and the Ca^{2+} cations within C-(N-)A-S-H gel [32]. Since the C-(N-)A-S-H gel with higher Ca/Si or Ca/(Si+Al) ratios have a higher charge density, it is conceivable that the electrostatic interaction between the C-(N-)A-S-H gel and PVA fiber surface are enhanced. These stronger interactions finally result in a stronger adhesion, thus stronger chemical bonding at higher Ca/Si or Ca/(Si+Al) ratios in debonding scenarios I.

Secondly, our previous study on identical AASF matrices confirmed that the matrix fracture toughness (K_{Ic}) and the crack tip toughness (J_{tip}), i.e., the resistance of crack initiation in the AASF matrix, are also dominated by the Ca/Si and Ca/(Si+Al) ratios of the C-(N-)A-S-H gel [18]. Both K_{Ic} and J_{tip} as fracture properties of the matrix are fundamentally related to the interaction between the reaction product particles (i.e., cohesion). This is reasonable considering that C-(N-)A-S-H gel with high Ca/Si or Ca/(Si+Al) ratios present a high negative surface charge density [77], which leads to enhanced cohesion in the AASF matrix [18]. As a result, the stronger cohesion also leads to stronger chemical bonding energy at higher Ca/Si or Ca/(Si+Al) ratios in debonding scenarios II.

3.3.3 Origin of initial frictional bond τ_0 and slip-hardening behavior

The initial friction between the PVA fiber and AASF matrix can be described as “dry friction” between two solid surfaces. The classic coulomb-type friction law is thereby assumed to be applicable. The initial frictional bond τ_0 is then determined by (1) the surface properties of the two contact surfaces (normally characterized by the friction coefficient) and (2) the residual stress of the surrounding matrix onto the fiber surface [27, 80].

Firstly, the initial friction bond is stronger with a higher friction coefficient, which could be achieved by a higher fracture surface roughness of the AASF matrix. According to Lange et al. [81], the fracture surface roughness in a cementitious matrix is positively related to its fracture toughness (K_{Ic}). While in our study on identical AASF matrices, we found a strong positive linear relationship between matrix K_{Ic} and the Ca/Si ratio of C-(N-)A-S-H gel [18]. As a result, AASF matrices with high Ca/Si ratios are expected to have a higher friction coefficient, which contributes to a stronger initial friction bond. This

consistency of the initial friction and K_{Ic} has also been reported previously by Nematollahi et al. [24] in fly ash-based SHGC.

Secondly, the residual stress of the surrounding matrix onto the fiber surface also affect the initial friction bond τ_0 [82]. This residual stress is caused by shrinkage of the AASF matrix, such as autogenous and/or possible drying shrinkage. Naturally, it is also affected by the creep and relaxation behavior of the AASF matrix. Given the fact that the shrinkage and creep are governed by various factors (such as pore structure, mechanical properties, and most likely chemical composition of the reaction products [83, 84]), further insight into the mechanism of shrinkage and creep in AASF systems are needed to better understand the residual stress and the related friction behavior.

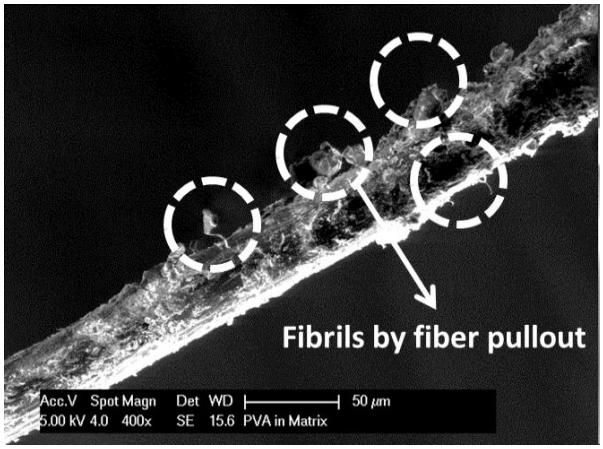

Figure 15 Fibrils on PVA fiber surface after single-fiber pullout test

The slip-hardening behavior results from the lower rigidity of the PVA fiber in comparison to the surrounding AASF matrix, leading to severe abrasion between the PVA fiber and the surrounding rough AASF matrix tunnel. The SEM micrograph in Figure 15 shows the surface of the pulled-out PVA fiber contain a substantial amount of fibrils as well as spalled micro-debris from the matrix attached to the fibrils. This is a result of the abrasion, which results in “micro-excavation” damage to the PVA fiber surface and leaves the fiber debris in the form of stripped fibrils [43]. With increasing fiber pullout displacement, the accumulation of these fibrils (with matrix micro-debris) promotes the formation of a “locking front”, which increases the pullout resistance [85]. This effect is also referred to as the “jamming effect” [29, 43]. The slip-hardening behavior may lead to a tensile load exceeding the fiber tensile strength causing rupture of the fiber. This rupture happens when the pullout load reaches the maximum P_{max} as shown in Figure 4 (b).

The slip-hardening behavior of PVA fiber is influenced by at least three factors: fiber/matrix adhesion, matrix surface roughness, and shrinkage-induced residual stress. The adhesion between the PVA fiber and the matrix plays a crucial role in preventing *adhesive* failure at the fiber/matrix interface (Scenario I in Section 3.3.1), which in turn allows for the initiation of "micro-excavation". Additionally, the higher surface roughness of the matrix, reflected by the matrix fracture toughness (K_{Ic}), can promote the “micro-excavation” damage at fiber surface. This results in a higher resistance during the

pullout process due to a more severe fiber-matrix interaction. Finally, the shrinkage-induced residual stress on the fiber surface contributes to the accumulation of fibrils and formation of a "locking front," leading to increased pullout resistance.

3.3.4 Implications on the development of strain-hardening geopolymer composites (SHGC)

The findings of this study have significant implications for the advancement of new strain-hardening geopolymer composite (SHGC). The fiber/matrix interfacial transition zone (ITZ) observed in this study is dense and has low porosity. Moreover, the stronger chemical bonding (Section 3.1.2) suggests that PVA fibers embedded in an alkali-activated matrix might be more susceptible to fiber rupture during the pullout process than those in cementitious matrices. As a result, special attention should be given to designing suitable chemical bonding energy (G_d) to improve the fiber's bridging capacity during the stages of crack initiation and propagation, and thereby the composite performance [86].

In cementitious system, the most convenient and effective approach to modify the chemical bonding is to incorporate supplementary cementitious materials (SCMs) into the cementitious matrix [30]. The modification of the fiber surface is also effective [29], yet it is considered difficult for a commercially available product like PVA fibers. Furthermore, the relationships between SCM content and surface characteristics (e.g., surface oiling) to the G_d is also complicated to establish. Fortunately, the chemical bonding of PVA fiber in alkali-activated system can be more conveniently adjusted compared to cementitious system. The strong linear correlation between G_d and Ca/Si of the C-(N-)A-S-H gel in alkali-activated matrix identified in this study (Figure 14) offers useful guidance to adjust the chemical bonding. In the case of AASF, this could be achieved by changing the ratio between slag/fly ash (Ca content) and the silicate modulus in the alkaline activator (Si content). Considering that the Ca/Si ratio of C-(N-)A-S-H gel has a wide range to be adjusted (0.3 to 0.8), the findings offer clear guidance and also freedom for researchers and engineers to tailor the chemical bonding energy G_d by adjusting the mixture design of alkali-activated matrix. Particularly, they are valuable for mixture development that require accurate engineering of interface bonding properties for a satisfactory performance of high-performance alkali-activated composite such as SHGC.

4. Conclusions

This paper presents a systematic experimental investigation of the PVA fiber/matrix interface bonding properties in AASF pastes. The influence of PVA fiber on the microstructure and the reaction product formation within the ITZ were also characterized. Based on the experimental results, the relationship between chemical bonding and the chemical composition of the C-(N-)A-S-H gel as main reaction product was further explored. The origin of the initial frictional bond and slip-hardening behavior of PVA fiber in AASF pastes were also discussed. Based on the results and discussions, the following conclusions can be drawn:

- The chemical bonding energy G_d between PVA fiber and AASF matrix increases with increasing Ca/Si and Ca/(Si/+Al) ratio of C-(N-)A-S-H gel, the main reaction product in AASF pastes.
- The hydrophilic nature of PVA fiber promotes the formation of a high-Ca C-(N-)A-S-H phase near the PVA fiber surface. This high-Ca C-(N-)A-S-H phase has considerably higher Ca/Si and Ca/(Si+Al) ratios, similar Al/Si ratios, and lower Mg/Ca ratios compared to the C-(N-)A-S-H phases in the bulk matrix.
- C-(N-)A-S-H and C-(N-)A-S-H+Ht phases were formed in the bulk matrix of AASF pastes. The main difference between them is their different Mg content due to the different amounts of hydrotalcite intermixed within C-(N-)A-S-H phases.
- Because of the strong chemical bond between PVA fiber and AASF matrix, the debonding process is dominated by the *cohesive* failure that happened within the ITZ rather than the *adhesive* failure along the PVA fiber surface. As a result, the initial friction bond τ_0 is primarily determined by the interaction between the fracture surfaces of the AASF matrix and not between PVA fiber and the AASF matrix.
- The initial frictional bond τ_0, unlike the chemical bonding energy G_d, is not only determined by the chemical composition of the reaction products. A synergistic mechanism of the fracture surface roughness of the matrix (positively related to K_{Ic}) and shrinkage-induced residual stress determines the magnitude of the frictional resistance.
- The slip-hardening behavior of PVA fiber in the AASF matrix is caused by a 'jamming' effect. The accumulation of the stripped fibrils (along with matrix micro-debris) identified on the fiber surface increases the pullout resistance.
- The study provides important insights into the interface bonding properties of PVA fiber in AASF matrix. It also provides able guidance for tailoring the interface bonding properties and thus the development of high-performance alkali-activated composites such as strain-hardening geopolymer composite (SHGC).

Acknowledgments

This research was carried out in Microlab, Delft University of Technology and was financially supported by the Netherlands Organization for Scientific Research (NWO), Grant No.729.001.013 and National Natural Science Foundation of China (NSFC), Grant No. 5151101050. The authors would like to thank Dr. Lupita Sierra-Beltran, Dr. Jishen Qiu, and Dr. Haoliang Wu for the discussion on the single-fiber pullout tests set-up, Prof. Victor C. Li, Prof. Erik Schlangen, and Dr. Jorge Dolado for the discussion on interface properties, and Paul Veerman for helping with the set-up of single-fiber pullout

572 tests. Additionally, the authors wish to acknowledge Kuraray Co., Ltd Japan for supplying the PVA
573 fiber.

574 References

575 [1] C. Shi, D. Roy, P. Krivenko, Alkali-activated cements and concretes, CRC press2006.

576 [2] J. Davidovits, Geopolymers, J Therm Anal, 37 (1991) 1633-1656.

577 [3] J.L. Provis, S.A. Bernal, Geopolymers and related alkali-activated materials, Annu Rev Mater Res, 44 (2014)
578 299-327.

579 [4] G. Habert, C. Ouellet-Plamondon, Recent update on the environmental impact of geopolymers, RILEM
580 technical Letters, 1 (2016) 17-23.

581 [5] P. Duxson, J.L. Provis, G.C. Lukey, J.S. Van Deventer, The role of inorganic polymer technology in the
582 development of 'green concrete', Cement and Concrete Research, 37 (2007) 1590-1597.

583 [6] K. Arbi, M. Nedeljkovic, Y. Zuo, G. Ye, A Review on the Durability of Alkali-Activated Fly Ash/Slag Systems:
584 Advances, Issues, and Perspectives, Ind Eng Chem Res, 55 (2016) 5439-5453.

585 [7] M. Albitar, M.M. Ali, P. Visintin, M. Drechsler, Durability evaluation of geopolymer and conventional concretes,
586 Construction and Building Materials, 136 (2017) 374-385.

587 [8] F. Pacheco-Torgal, Z. Abdollahnejad, A. Camões, M. Jamshidi, Y. Ding, Durability of alkali-activated binders:
588 a clear advantage over Portland cement or an unproven issue?, Construction and Building Materials, 30 (2012)
589 400-405.

590 [9] J. Zhang, C. Shi, Z. Zhang, Z. Ou, Durability of alkali-activated materials in aggressive environments: A
591 review on recent studies, Construction and Building Materials, 152 (2017) 598-613.

592 [10] A. Palomo, O. Maltseva, I. Garcia-Lodeiro, A. Fernández-Jiménez, Portland Versus Alkaline Cement:
593 Continuity or Clean Break: "A Key Decision for Global Sustainability", Frontiers in Chemistry, 9 (2021).

594 [11] J. Van Deventer, J. Provis, P. Duxson, G. Lukey, Reaction mechanisms in the geopolymeric conversion of
595 inorganic waste to useful products, Journal of hazardous materials, 139 (2007) 506-513.

596 [12] P. Duxson, J.L. Provis, G.C. Lukey, J.S.J. van Deventer, The role of inorganic polymer technology in the
597 development of 'green concrete', Cem. Concr. Res., 37 (2007) 1590-1597.

598 [13] I. Ismail, S.A. Bernal, J.L. Provis, R. San Nicolas, S. Hamdan, J.S. van Deventer, Modification of phase
599 evolution in alkali-activated blast furnace slag by the incorporation of fly ash, Cement and Concrete Composites,
600 45 (2014) 125-135.

601 [14] F. Puertas, A. Fernández-Jiménez, Mineralogical and microstructural characterisation of alkali-activated fly
602 ash/slag pastes, Cement and Concrete composites, 25 (2003) 287-292.

603 [15] N.K. Lee, H.K. Lee, Reactivity and reaction products of alkali-activated, fly ash/slag paste, Construction and
604 Building Materials, 81 (2015) 303-312.

605 [16] S. Puligilla, P. Mondal, Role of slag in microstructural development and hardening of fly ash-slag
606 geopolymer, Cement and Concrete Research, 43 (2013) 70-80.

607 [17] S. Zhang, A. Keulen, K. Arbi, G. Ye, Waste glass as partial mineral precursor in alkali-activated slag/fly ash
608 system, Cement and Concrete Research, 102 (2017) 29-40.

609 [18] S. Zhang, Z. Li, B. Ghiassi, S. Yin, G. Ye, Fracture properties and microstructure formation of hardened
610 alkali-activated slag/fly ash pastes, Cement and Concrete Research, 144 (2021) 106447.

611 [19] P.K. Sarker, R. Haque, K.V. Ramgolam, Fracture behaviour of heat cured fly ash based geopolymer
612 concrete, Materials & Design, 44 (2013) 580-586.

613 [20] Z. Pan, J.G. Sanjayan, B.V. Rangan, Fracture properties of geopolymer paste and concrete, Mag Concrete
614 Res, 63 (2011) 763-771.

615 [21] R.J. Thomas, S. Peethamparan, Alkali-activated concrete: Engineering properties and stress–strain
616 behavior, Construction and Building Materials, 93 (2015) 49-56.

617 [22] C.D. Atiş, C. Bilim, Ö. Çelik, O. Karahan, Influence of activator on the strength and drying shrinkage of
618 alkali-activated slag mortar, Construction and building materials, 23 (2009) 548-555.

619 [23] M. Ohno, V.C. Li, An integrated design method of Engineered Geopolymer Composite, Cement and
620 Concrete Composites, 88 (2018) 73-85.

621 [24] B. Nematollahi, J. Qiu, E.-H. Yang, J. Sanjayan, Microscale investigation of fiber-matrix interface properties
622 of strain-hardening geopolymer composite, Ceramics International, 43 (2017) 15616-15625.

623 [25] S. Zhang, V.C. Li, G. Ye, Micromechanics-guided development of a slag/fly ash-based strain-hardening
624 geopolymer composite, Cement and Concrete Composites, 109 (2020) 103510.

625 [26] B. Nematollahi, J. Sanjayan, J. Qiu, E.-H. Yang, Micromechanics-based investigation of a sustainable
626 ambient temperature cured one-part strain hardening geopolymer composite, Construction and Building
627 Materials, 131 (2017) 552-563.

628 [27] V.C. Li, H. Stang, Interface property characterization and strengthening mechanisms in fiber reinforced
629 cement based composites, Adv Cem Based Mater, 6 (1997) 1-20.

630 [28] C. Redon, V.C. Li, C. Wu, H. Hoshiro, T. Saito, A. Ogawa, Measuring and modifying interface properties of
631 PVA fibers in ECC matrix, Journal of Materials in Civil Engineering, 13 (2001) 399-406.

632 [29] V.C. Li, C. Wu, S. Wang, A. Ogawa, T. Saito, Interface tailoring for strain-hardening polyvinyl alcohol-
633 engineered cementitious composite (PVA-ECC), ACI Materials Journal, 99 (2002) 463-472.

634 [30] E.-H. Yang, Y. Yang, V.C. Li, Use of high volumes of fly ash to improve ECC mechanical properties and
635 material greenness, ACI materials journal, 104 (2007) 620-628.

636 [31] A.C. Constâncio Trindade, I. Curosu, M. Liebscher, V. Mechtcherine, F. de Andrade Silva, On the
637 mechanical performance of K- and Na-based strain-hardening geopolymer composites (SHGC) reinforced with
638 PVA fibers, Construction and Building Materials, 248 (2020) 118558.

639 [32] S. Zhang, E. Duque-Redondo, A. Kostiuchenko, J.S. Dolado, G. Ye, Molecular dynamics and experimental
640 study on the adhesion mechanism of polyvinyl alcohol (PVA) fiber in alkali-activated slag/fly ash, Cement and
641 Concrete Research, 145 (2021) 106452.

642 [33] L. Kuraray Co., Kuralon K-II characteristics and properties.

643 [34] X. Gao, Q.L. Yu, H.J.H. Brouwers, Reaction kinetics, gel character and strength of ambient temperature
644 cured alkali activated slag–fly ash blends, Construction and Building Materials, 80 (2015) 105-115.

645 [35] A. Katz, V.C. Li, A special technique for determining the bond strength of micro-fibres in cement matrix by
646 pullout test, J Mater Sci Lett, 15 (1996) 1821-1823.

647 [36] Z. Lin, T. Kanda, V. Li, On interfaCe prOperty CharaCteriZatiOn and performance Of fiber-reinforCed
648 Cementitious COII pOSileS, Concrete Science and Engineering, 1 (1999) 173-174.

649 [37] A.R. Sakulich, V.C. Li, Nanoscale characterization of engineered cementitious composites (ECC), Cement
650 and Concrete Research, 41 (2011) 169-175.

651 [38] K. Scrivener, R. Snellings, B. Lothenbach, A practical guide to microstructural analysis of cementitious
652 materials, CRC Press2018.

653 [39] D. West, Principal component analysis in EDS: the COMPASS algorithm, Thermo Fisher Scientific white
654 paper WP52773, 2015.

655 [40] P.G. Kotula, M.R. Keenan, Application of multivariate statistical analysis to STEM X-ray spectral images:
656 Interfacial analysis in microelectronics, Microscopy and Microanalysis, 12 (2006) 538-544.

657 [41] K. Thompson, Large-Area Quantitative Phase Mapping in the Scanning Electron Microscope, Microscopy
658 Today, 25 (2017) 36-45.

659 [42] I. Curosu, V. Mechtcherine, O. Millon, Effect of fiber properties and matrix composition on the tensile
660 behavior of strain-hardening cement-based composites (SHCCs) subject to impact loading, Cement and
661 Concrete Research, 82 (2016) 23-35.

662 [43] Z. Lin, V.C. Li, Crack bridging in fiber reinforced cementitious composites with slip-hardening interfaces, J
663 Mech Phys Solids, 45 (1997) 763-787.

664 [44] E.-H. Yang, S. Wang, Y. Yang, V.C. Li, Fiber-bridging constitutive law of engineered cementitious
665 composites, Journal of advanced concrete technology, 6 (2008) 181-193.

666 [45] S.-D. Wang, K.L. Scrivener, P.L. Pratt, Factors affecting the strength of alkali-activated slag, Cement and
667 Concrete Research, 24 (1994) 1033-1043.

668 [46] C. Shi, P. Xie, Interface between cement paste and quartz sand in alkali-activated slag mortars, Cement
669 and Concrete Research, 28 (1998) 887-896.

670 [47] R. San Nicolas, J.L. Provis, The interfacial transition zone in alkali-activated slag mortars, Frontiers in
671 Materials, 2 (2015) 70.

672 [48] T. Horikoshi, A. Ogawa, T. Saito, H. Hoshiro, G. Fischer, V. Li, Properties of Polyvinylalcohol fiber as
673 reinforcing materials for cementitious composites, International RILEM workshop on HPFRCC in structural
674 applications, 2006, pp. 147.

675 [49] T. Chu, R. Robertson, H. Najm, A. Naaman, Effects of poly (vinyl alcohol) on fiber cement interfaces. Part
676 II: Microstructures, Adv Cem Based Mater, 1 (1994) 122-130.

677 [50] P. Xu, Q. Zhao, W. Qiu, Y. Xue, N. Li, Microstructure and Strength of Alkali-Activated Bricks Containing
678 Municipal Solid Waste Incineration (MSWI) Fly Ash Developed as Construction Materials, Sustainability, 11
679 (2019) 1283.

680 [51] R.J. Myers, S.A. Bernal, J.L. Provis, A thermodynamic model for C-(N-) ASH gel: CNASH_ss. Derivation
681 and validation, Cement and Concrete Research, 66 (2014) 27-47.

682 [52] R.J. Myers, B. Lothenbach, S.A. Bernal, J.L. Provis, Thermodynamic modelling of alkali-activated slag
683 cements, Applied Geochemistry, 61 (2015) 233-247.

684 [53] Y. Zuo, Experimental Study and Numerical Simulation of the Reaction Process and Microstructure
685 Formation of Alkali-Activated Materials, Delft University of Technology, 2019.

686 [54] M. Nedeljković, Carbonation mechanism of alkali-activated fly ash and slag materials: In view of long-term
687 performance predictions, Delft University of Technology, 2019.

[55] A. Keulen, Q.L. Yu, S. Zhang, S. Grünewald, Effect of admixture on the pore structure refinement and enhanced performance of alkali-activated fly ash-slag concrete, Construction and Building Materials, 162 (2018) 27-36.

[56] H. Ye, A. Radlińska, Fly ash-slag interaction during alkaline activation: Influence of activators on phase assemblage and microstructure formation, Construction and building materials, 122 (2016) 594-606.

[57] M. Ben Haha, G. Le Saout, F. Winnefeld, B. Lothenbach, Influence of activator type on hydration kinetics, hydrate assemblage and microstructural development of alkali activated blast-furnace slags, Cement and Concrete Research, 41 (2011) 301-310.

[58] H. Ye, Nanoscale attraction between calcium-aluminosilicate-hydrate and Mg-Al layered double hydroxides in alkali-activated slag, Materials Characterization, 140 (2018) 95-102.

[59] Z. Jia, C. Chen, H. Zhou, Y. Zhang, The characteristics and formation mechanism of the dark rim in alkali-activated slag, Cement and Concrete Composites, 112 (2020) 103682.

[60] M. Yio, J. Phelan, H. Wong, N. Buenfeld, Determining the slag fraction, water/binder ratio and degree of hydration in hardened cement pastes, Cement and concrete research, 56 (2014) 171-181.

[61] Y. Zhang, O. Çopuroğlu, Role of the grain size on the hydration characteristics of slag in an aged field concrete, Cement and Concrete Research, 162 (2022) 106985.

[62] Q. Wang, D. O'Hare, Recent advances in the synthesis and application of layered double hydroxide (LDH) nanosheets, Chem Rev, 112 (2012) 4124-4155.

[63] C. van Hoek, J. Small, S. van der Laan, Large-Area Phase Mapping Using PhAse Recognition and Characterization (PARC) Software, Microscopy Today, 24 (2016) 12-21.

[64] D. Hild, P. Schwartz, Plasma-treated ultra-high strength polyethylene fibers. Part II. Increased adhesion to poly (methyl methacrylate), Journal of adhesion science and technology, 6 (1992) 897-917.

[65] Y.-W. Chan, V.C. Li, Effects of transition zone densification on fiber/cement paste bond strength improvement, Adv Cem Based Mater, 5 (1997) 8-17.

[66] H. Wu, V.C. Li, Basic interfacial characteristic of polyethylene fiber/cement composites and its modification by plasma, (1997).

[67] B. Nematollahi, J. Sanjayan, J. Qiu, E.-H. Yang, High ductile behavior of a polyethylene fiber-reinforced one-part geopolymer composite: A micromechanics-based investigation, Arch Civ Mech Eng, 17 (2017) 555-563.

[68] S. He, Z. Li, E.-H. Yang, Quantitative characterization of anisotropic properties of the interfacial transition zone (ITZ) between microfiber and cement paste, Cement and Concrete Research, 122 (2019) 136-146.

[69] Z. Lu, R. Yin, J. Yao, C.K.Y. Leung, Surface modification of polyethylene fiber by ozonation and its influence on the mechanical properties of Strain-Hardening Cementitious Composites, Compos Part B-Eng, 177 (2019) 107446.

[70] Z. Lu, J. Yao, C.K.Y. Leung, Using graphene oxide to strengthen the bond between PE fiber and matrix to improve the strain hardening behavior of SHCC, Cement and Concrete Research, 126 (2019) 105899.

[71] A. Drechsler, R. Frenzel, A. Caspari, S. Michel, M. Holzschuh, A. Synytska, I. Curosu, M. Liebscher, V. Mechtcherine, Surface modification of poly(vinyl alcohol) fibers to control the fiber-matrix interaction in composites, Colloid Polym Sci, 297 (2019) 1079-1093.

[72] S. Zhang, B. Ghiassi, G. Ye, Experimental study on the interface properties of PVA fibers in slag/fly ash based geopolymer pastes, 4th International Conference on Service Life Design for Infrastructures, Rilem2018, pp. 739-745.

730 [73] W. Zhang, X. Zou, F. Wei, H. Wang, G. Zhang, Y. Huang, Y. Zhang, Grafting SiO2 nanoparticles on polyvinyl
731 alcohol fibers to enhance the interfacial bonding strength with cement, Compos Part B-Eng, 162 (2019) 500-
732 507.

733 [74] S. Zhang, Y. Zuo, Z. Li, G. Ye, Isothermal calorimetric study on heat evolution and of apparent activation
734 energy of alkali-activated slag/fly ash pastes, 2th International Conference on Sustainable Building
735 MaterialsEindhoven, the Netherlands, 2019.

736 [75] D. Ravikumar, N. Neithalath, Effects of activator characteristics on the reaction product formation in slag
737 binders activated using alkali silicate powder and NaOH, Cement and Concrete Composites, 34 (2012) 809-
738 818.

739 [76] D. Ravikumar, N. Neithalath, Reaction kinetics in sodium silicate powder and liquid activated slag binders
740 evaluated using isothermal calorimetry, Thermochim Acta, 546 (2012) 32-43.

741 [77] C. Labbez, I. Pochard, B. Jönsson, A. Nonat, C-S-H/solution interface: Experimental and Monte Carlo
742 studies, Cement and Concrete Research, 41 (2011) 161-168.

743 [78] D. Hou, J. Yu, P. Wang, Molecular dynamics modeling of the structure, dynamics, energetics and
744 mechanical properties of cement-polymer nanocomposite, Compos Part B-Eng, 162 (2019) 433-444.

745 [79] Y. Zhou, L. Tang, J. Liu, C. Miao, Interaction mechanisms between organic and inorganic phases in calcium
746 silicate hydrates/poly(vinyl alcohol) composites, Cement and Concrete Research, 125 (2019) 105891.

747 [80] A. Naaman, G. Namur, H. Najm, J. Alwan, Bond mechanisms in fiber reinforced cement-based composites,
748 MICHIGAN UNIV ANN ARBOR DEPT OF CIVIL ENGINEERING, 1989.

749 [81] D.A. Lange, H.M. Jennings, S.P. Shah, Relationship between fracture surface roughness and fracture
750 behavior of cement paste and mortar, Journal of the American Ceramic Society, 76 (1993) 589-597.

751 [82] N. Hadjis, M. Piggott, The effect of matrix stresses on fibre pull-out forces, Journal of Materials Science, 12
752 (1977) 358-364.

753 [83] H. Ye, A. Radlińska, Shrinkage mechanisms of alkali-activated slag, Cement and Concrete Research, 88
754 (2016) 126-135.

755 [84] Z. Li, T. Lu, X. Liang, H. Dong, G. Ye, Mechanisms of autogenous shrinkage of alkali-activated slag and fly
756 ash pastes, Cement and Concrete Research, 135 (2020) 106107.

757 [85] M. Ranjbarian, V. Mechtcherine, Z. Zhang, I. Curosu, J. Storm, M. Kaliske, Locking Front Model for pull-out
758 behaviour of PVA microfibre embedded in cementitious matrix, Cement and Concrete Composites, (2019).

759 [86] V.C. Li, Micromechanics and Engineered Cementitious Composites (ECC) Design Basis, Engineered
760 Cementitious Composites (ECC), Springer2019, pp. 11-71.

761